

# Search for Nucleon Decay with Final States $\ell^+\eta^0$ , $\bar{\nu}\eta^0$ , and $\bar{\nu}\pi^{+,0}$ Using Soudan 2

D. Wall<sup>5,a</sup>, W.W.M. Allison<sup>3</sup>, G.J. Alner<sup>4</sup>, D.S. Ayres<sup>1</sup>, W.L. Barrett<sup>6</sup>,  
C. Bode<sup>2</sup>, P.M. Border<sup>2</sup>, J.H. Cobb<sup>3</sup>, R. Cotton<sup>4</sup>, H. Courant<sup>2</sup>, J. Chung<sup>5</sup>,  
D.M. Demuth<sup>2</sup>, T.H. Fields<sup>1</sup>, H.R. Gallagher<sup>3</sup>, M.C. Goodman<sup>1</sup>, R. Gran<sup>2</sup>,  
T. Joffe-Minor<sup>1</sup>, T. Kafka<sup>5</sup>, S.M.S. Kasahara<sup>2</sup>, W. Leeson<sup>1</sup>, P.J. Litchfield<sup>4</sup>,  
W.A. Mann<sup>5</sup>, M.L. Marshak<sup>2</sup>, R.H. Milburn<sup>5</sup>, W.H. Miller<sup>2</sup>, L. Mualem<sup>2</sup>,  
A. Napier<sup>5</sup>, W.P. Oliver<sup>5</sup>, G.F. Pearce<sup>4</sup>, E.A. Peterson<sup>2</sup>, D.A. Petyt<sup>4</sup>,  
L.E. Price<sup>1</sup>, K. Ruddick<sup>2</sup>, M. Sanchez<sup>5</sup>, J. Schneps<sup>5</sup>, A. Stassinakis<sup>3</sup>,  
J.L. Thron<sup>1</sup>, S.P. Wakely<sup>2</sup>, N. West<sup>3</sup>

<sup>1</sup>*Argonne National Laboratory, Argonne, IL 60439*

<sup>2</sup>*University of Minnesota, Minneapolis, MN 55455*

<sup>3</sup>*Department of Physics, University of Oxford, Oxford OX1 3RH, UK*

<sup>4</sup>*Rutherford Appleton Laboratory, Chilton, Didcot, Oxfordshire OX11 0QX, UK*

<sup>5</sup>*Tufts University, Medford, MA 02155*

<sup>6</sup>*Western Washington University, Bellingham, WA 98225*

<sup>a</sup>Now at Sapien Corporation, One Memorial Drive, Cambridge, MA 02142

## Abstract

We have searched for nucleon decay into five two-body final states using a 4.4 kiloton-year fiducial exposure of the Soudan 2 iron tracking calorimeter. For proton decay into the fully visible final states  $\mu^+\eta^0$  and  $e^+\eta^0$ , we observe zero and one event, respectively, that satisfy our search criteria for nucleon decay. The lifetime lower limits ( $\tau/B$ ) thus implied are  $89 \times 10^{30}$  years and  $81 \times 10^{30}$  years at 90% confidence level. For neutron decay into  $\bar{\nu}\eta^0$ , we obtain the lifetime lower limit  $71 \times 10^{30}$  years. Limits are also reported for neutron decay into  $\bar{\nu}\pi^0$ , and for proton decay into  $\bar{\nu}\pi^+$ .

PACS numbers: 11.30.Fs, 12.20.Fv, 11.30.Pb, 14.20.Dh

## I. INTRODUCTION

### A. SUSY predictions for nucleon decay

The decay of the nucleon is a possible experimental window into fundamental processes at high mass scales. Calculations carried out in supersymmetric (SUSY) grand unified theories (GUTs), such as SUSY SU(5) and SUSY SO(10), have become increasingly more detailed, and predicted lifetimes are within a range which may be accessible to experiment. In contrast to their non-SUSY precursors, SUSY GUT models generally favor decay modes with final state  $K^0$  or  $K^+$  mesons. Some of these models also predict that other decay modes may exhibit a significant branching fraction. The latter modes include the lepton plus eta meson and the  $\bar{\nu}\pi$  modes. In SUSY SU(5) models, lifetimes predicted for  $\ell^+\eta$  and  $\bar{\nu}\eta$  are longer than those for  $\bar{\nu}K$  or  $\bar{\nu}\pi$  modes by factors which vary from 2-3 to one or two orders of magnitude [1–3]. Eta mode lifetimes which are hundreds of times longer than  $\bar{\nu}K$  or  $\ell^+K$  lifetimes have also been predicted in SUSY SO(10) [4,5]. However, it has been proposed [6,7] that in SUSY GUTs such as SO(10), there exists a new set of color triplets and thereby a new source of  $d=5$  operators which may allow  $p \rightarrow \ell^+\eta$  to become prominent (along with  $\bar{\nu}K^+$  and  $\bar{\nu}\pi^+$ ). In SUSY GUTs the  $\bar{\nu}\pi$  modes are usually predicted to have decay lifetimes which are longer than  $\bar{\nu}K$  modes. In specific models, however, it is possible for interference between third and second generation amplitudes to alter this situation so that  $\bar{\nu}\pi$  modes become dominant [1,3].

We have previously searched for nucleon decay final states with strangeness using the Soudan 2 iron tracking calorimeter and reported the results as lifetime lower limits [8,9]. In this work, we extend our investigations to include the  $\ell^+\eta^0$ ,  $\bar{\nu}\eta^0$ ,  $\bar{\nu}\pi^0$ , and  $\bar{\nu}\pi^+$  final states.

### B. Previous searches for $\ell^+\eta$ , $\bar{\nu}\eta^0$ , and $\bar{\nu}\pi$ modes

Two-body  $\ell^{+,0}\eta$  and  $\bar{\nu}\pi$  decays of nucleons were regarded as interesting in the context of non-SUSY GUT models, and experimental searches were reported at various times during the past two decades. Multiple ring topologies were investigated for  $\ell^+\eta$ ,  $\bar{\nu}\eta$ , and  $\bar{\nu}\pi^0$  final states by the IMB and Kamiokande water Cherenkov experiments [10–12]. In the HPW water Cherenkov experiment, events exhibiting a two muon decay signature were examined for compatibility with  $p \rightarrow \mu^+\eta$ , with  $\eta$  decaying to  $\pi^+\pi^-\pi^0$  or  $\pi^+\pi^-\gamma$  [13]. The  $\ell^+\eta$ ,  $\bar{\nu}\eta$ , and  $\bar{\nu}\pi$  modes were also investigated using the planar iron tracking calorimeter of Fréjus [14,15]. More recently, substantial improvement of lifetime limits for the two-body eta modes has been reported, based upon the 7.6 kton-year exposure of the IMB-3 water Cherenkov detector [16]. Generally, these experiments observed zero or modest numbers of candidate events. Understandably, the more loosely constrained  $n \rightarrow \bar{\nu}\eta$  and  $n \rightarrow \bar{\nu}\pi^0$  modes were found to exhibit more background and consequently to yield less stringent lifetime lower limits.

## II. DETECTOR AND EVENT SAMPLES

## A. Central Detector and Active Shield

Soudan 2 is a massive 963 (809 fiducial) metric-ton iron tracking calorimeter. It operates as a slow-drift, fine-grained, time projection chamber of honeycomb-lattice geometry and with  $dE/dx$  imaging of tracks and showers. As such, it differs considerably from water Cherenkov detectors and from planar iron tracking calorimeters.

The construction and performance of the Soudan calorimeter are described in previous publications [17]. In brief, charged particles are imaged via one meter long, slightly conductive, plastic drift tubes. Electrons liberated by throughgoing charged particles drift to the tube ends under the action of a voltage gradient applied along the tubes. The tubes are sandwiched between mylar sheets so as to comprise a “bandolier” assembly. Corrugated steel sheets with interleaved bandolier are then stacked to form a massive lattice. A stack is packaged with wireplanes and cathode pickup strips at the drift tube ends and surrounded by thin steel skins which provide the gas enclosure. The resulting assemblies are  $1 \times 1 \times 2.5$  m, 4.3 ton calorimeter modules. The tracking calorimeter is constructed building-block fashion, with contiguous “walls” which are two modules high and eight modules wide. The calorimeter is surrounded on all sides by a double-layer, cavern-liner proportional tube active shield of 1700 m<sup>2</sup> total tracking area [18]. Shield augmentations in the form of additional single layers and a double-layer top cover of proportional tubes have been operational since 1995.

For the task of searching for nucleon decay in a variety of final states, the Soudan 2 calorimeter provides imaging of non-relativistic as well as relativistic tracks, and its systematics are different from those of other experiments. The detector is located at a depth of 713 meters (2070 mwe) in the Tower-Soudan Underground Mine State Park in northern Minnesota. Data-taking is still underway, having commenced in April 1989 when the total mass was 275 tons, and continued as more modules were installed. Operation with the calorimeter at full mass was first achieved in November 1993. The analysis reported in this work is based on a total (fiducial) exposure of 5.52 (4.41) kiloton-years, obtained with data taken through October 1998.

## B. Data and Monte Carlo event samples

Four distinct event samples have been assembled for this analysis; two of the samples are generated as Monte Carlo (MC) simulations with full detector response, and two are comprised of data events recorded in the experiment. These samples, details of which have been presented elsewhere [8,9], are:

- i) Nucleon decay MC:* For each of the nucleon decay processes investigated, we use MC simulations which track all final state particles through the detector geometry. Electronic hits are generated, and detector noise is included, in the same format as with real data.
- ii) Atmospheric neutrino MC:* Events are generated representing charged current and neutral current reactions which are initiated by the flux of atmospheric neutrinos. The neutrino MC program is based upon the flux calculation of the

Bartol group for the Soudan site [19]. The neutrino MC sample analyzed here corresponds to an exposure of 24.0 fiducial kton-years.

- iii) *Rock data:* We analyze events for which the veto shield recorded coincident, double-layer hits. Such events originate with inelastic cosmic-ray muon interactions in the cavern rock surrounding the detector. These shield-tagged “rock” events provide a reference sample by which to gauge cosmic-ray induced background events which are included in the “gold data”. The latter events arise either from shield inefficiency or from instances where an energetic neutral particle emerged from the cavern walls with no accompanying charged particles.
- iv) *Gold data:* Data events for which the cavern-liner active shield array was quiet during the allowed time window comprise our “gold event” sample. These events are mostly reactions initiated by atmospheric neutrinos but may contain nucleon decays, as well as the muon induced rock events with no shield hits (described above). The events of interest for our study are those with a “multiprong” topology, having two or more particles (other than recoil nucleons) emerging from the primary vertex. They are distinct from the more populous single-track and single-shower events which originate predominantly from neutrino quasi-elastic reactions.

Events of all four samples are required to be fully contained in a fiducial volume which is everywhere 20 cm or more from the outer surfaces of the calorimeter. In order for an event to be included in any of the above four samples it must survive the selections of a standard processing chain. At the head of the chain are the requirements imposed by the hardware trigger; events satisfying these requirements are subjected to a containment filter code. Events which survive are subjected to two successive scanning passes carried out by physicists; each pass involves three complete, independent scans. In the first scan pass, events with multiprong topologies used in this study are found with an overall efficiency of  $0.98^{+0.02}_{-0.04}$ . Descriptions of our hardware and software selections, and of our scanning procedures are given elsewhere [8,9,20]. Our procedures ensure that MC simulation events pass through identical or otherwise equivalent (e.g. the hardware trigger is implemented via software for MC events) steps in the chain [9].

Events which emerge from the second scan pass with a multiprong topology assignment are then reconstructed using an interactive graphics package. The set of reconstructed tracks and showers which comprises each event is subsequently entered into an event summary file from which kinematic quantities are calculated.

### C. Background from rock events and from neutrino interactions

Among the fully contained, multiprong events of our gold data sample, a small contribution may arise from cosmic ray induced rock events. These are events initiated by neutrons emerging from the cavern rock which impinge upon the central detector and which are unaccompanied by coincident hits in the surrounding shield array. In contrast to neutrino interactions or to nucleon decay, these shield-quiet rock events tend to occur at relatively

shallow penetration depths into the calorimeter. Their depth distribution, and their distribution in visible energy and in other variables, can be inferred from rock events tagged by coincident shield hits. To estimate the amount of zero-shield-hit rock background in our gold multiprongs sample, event distributions of gold data have been fitted to neutrino MC and shield-tagged rock samples using a multivariate discriminant analysis [9,21]. We find that, the fraction  $f$  of all multiprongs rock events which have at least one shield hit is  $f = 0.94 \pm 0.04$ .

For each individual nucleon decay channel, the same event selections applied to data multiprongs are also applied to the shield-tagged rock multiprongs. The zero-shield-hit rock background is then estimated as the product  $(1 - f)/f = 0.064$  times the number of shield-tagged rock events which satisfy the channel selections.

To calculate rates for background events in our nucleon decay search which arise from interactions of atmospheric neutrinos in the detector, we use our realistic neutrino MC simulation which is based upon atmospheric fluxes with null oscillations. The neutrino Monte Carlo program has been described in previous publications [9,20].

During the past decade, evidence for depletion of the atmospheric muon-neutrino flux as described by  $\nu_\mu \rightarrow \nu_x$  oscillations has become increasingly extensive; especially compelling are observations by Super-Kamiokande of zenith angle distortions in fluxes of both sub-GeV and multi-GeV muon neutrinos [22]. The disappearance of  $\nu_\mu$  flavor neutrinos by oscillations effectively reduces background in our search arising from  $(\nu_\mu + \bar{\nu}_\mu)$  charged-current reactions, and so a correction for this effect to our null oscillation estimates is warranted. To implement a correction we assume, as indicated by recent data, that  $\nu_x$  is an active neutrino which is not  $\nu_e$  (i.e.  $\nu_x = \nu_\tau$ ) [23]. Then, atmospheric neutrino oscillations do not affect background arising from  $(\nu_e + \bar{\nu}_e)$  charged-current reactions, nor do they affect background from neutral current reactions (initiated by any flavor). Consequently, to correct for  $\nu_\mu$  flavor disappearance, we simply scale the number of  $(\nu_\mu + \bar{\nu}_\mu)$  charged-current background events estimated from the null oscillation MC for each nucleon decay channel by the  $\nu_\mu/\nu_e$  flavor ratio  $R$  measured in the Soudan 2 experiment:  $R = 0.64 \pm 0.13$  [24]. As noted below in Sections IV and V, and in Table II, this correction yields small reductions in null oscillation background rates for  $p \rightarrow \mu^+\eta$  and  $p \rightarrow \bar{\nu}\pi^+$  final states. For  $p \rightarrow e^+\eta$  and  $n \rightarrow \bar{\nu}\pi^0$  channels however, the neutrino oscillation correction has negligible effect.

### III. NUCLEON DECAY SIMULATION AND SEARCH METHOD

#### A. Event generation

For each nucleon decay final state, a Monte Carlo sample is created and processed as described in Section II B. This sample is then used to determine the topological and kinematic properties that differentiate it from the atmospheric neutrino and the rock event backgrounds.

For each final state, about 500 events are generated and embedded into pulser trigger events from the detector which are taken at regular intervals throughout the exposure. In this way, the detector's evolving size and the background from natural radioactivity and cosmic rays are accurately incorporated into the simulation.

For two-body decay of a nucleon at rest, the final state momenta are uniquely determined. However, Fermi motion within parent iron and other nuclei of the calorimeter medium smears these momenta and thereby complicates final state identification. In our simulations, Fermi motion effects are modelled according to the parameterization of Ref. [25].

A Monte Carlo event for  $p \rightarrow \mu\eta$ ,  $\eta \rightarrow \gamma\gamma$ , which illustrates the search topology for this mode, is shown in Fig. 1. Here, the  $\mu^+$  appears as a single non-scattering track. The two gammas from  $\eta$  decay give rise to two showers which are spatially well separated and which point to the event vertex which is also the origin of the muon. The  $\mu^+$  endpoint decay - discernible in approximately 60% of events - appears in Fig. 1 as extra ionization “hits” (tube crossings) in the vicinity of the track’s range-out point.

In each nucleon decay mode, the meson can undergo intranuclear rescattering within the parent nucleus. For nuclei which have interior as well as surface nucleons ( $A \geq 12$ ), there is significant probability for event final states to be altered. For final state pions (in neutrino MC interactions as well as in nucleon decay), intranuclear rescattering is treated using a phenomenological cascade model [26]. Parameters of the model were set by requiring that the threshold pion production observed in  $\nu_\mu$ -deuteron ( $A = 2$ ) and  $\nu_\mu$ -neon ( $A = 20$ ) reactions be reproduced [27]. To account for the intranuclear rescattering of  $\eta$  mesons within iron nuclei we have adopted the survival fraction of 0.57 estimated by the Fréjus collaboration [14] using a detailed balance calculation. This value for the  $\eta^0$  survival is similar to the survival fraction of 0.52 which we calculate for the  $\pi^0$  of  $n \rightarrow \bar{\nu}\pi^0$  in iron nuclei. We note that a recent analysis of  $\eta$  meson photoproduction in nuclei finds the in-medium  $\eta N$  cross-section to be nearly independent of  $\eta$  momentum between 0 and 500 MeV/c [28].

## B. Search contour in the $M_{inv}$ versus $|\vec{p}_{net}|$ plane

Two quantities that are useful for selection of nucleon decay candidates and the rejection of backgrounds are the invariant mass,  $M_{inv}$ , and the magnitude of the net three-momentum,  $|\vec{p}_{net}|$ , of the reconstructed final state.

We create a scatter plot of invariant mass versus net event momentum for the reconstructed final states for each simulation. Then we choose a region in this plane whose boundary defines a kinematical selection which can be applied to the data and to the background samples. We observe that, for most nucleon decay final states, event distributions in each of these variables are approximately Gaussian. Consequently, the density distribution of points on the invariant mass versus momentum plane can be well represented by a bi-variate Gaussian probability distribution function. A detailed description of this construction is given elsewhere [9,29].

Projections of bi-variate Gaussian surfaces onto the  $M_{inv}$  versus  $|\vec{p}_{net}|$  plane for the eta modes of this search are shown in Figs. 2 – 7. In these figures, the distribution of a nucleon decay event population is depicted using five nested, elliptical boundaries. Proceeding outward from the innermost contour, the bounded regions contain respectively 10%, 30%, 50%, 70%, and 90% of the MC nucleon decay sample. From the five regions delineated we choose the 90%-of-sample contour - the outermost, solid-curve ellipse in Figs. 2–7 - to define our “primary” kinematic selection. That is, a candidate nucleon decay event has reconstructed

( $M_{inv}, |\vec{p}_{net}|$ ) values which lie within the outer contour. The interior contours (dashed ellipses in Figs. 2–7) are helpful to gauge whether an event sample as a whole exhibits the kinematics of nucleon decay, and for this reason we display them. For our search involving the  $\eta \rightarrow \gamma\gamma$  decay, containment within the 90% contour is our sole kinematic constraint; no subsidiary condition, such as a cut on the  $\gamma\gamma$  invariant mass, has been used.

All nucleon decay simulation events are subjected to the triggering requirements, the detector containment requirements, and to the scanning and topology cuts. Subsequently, kinematic cuts and additional topology cuts, designed to reduce the background on a mode-by-mode basis, are applied. The cumulative effect of these selections is to reduce the overall detection efficiency significantly. Typically, the product of the triggering, containment, and scanning selections reduces the survival fraction to below 30% for any mode. Table I shows the successive survival fractions (including  $\eta$  decay branching ratios) for all modes studied. Note that the effects of intranuclear rescattering processes (INR) are included in the survival fractions listed in Table I. For comparison, the rightmost column of Table I shows our estimates of  $\epsilon \times \text{BR}$  in the absence of INR within the iron and lighter nuclei (atomic masses 12 to 56) of the calorimeter medium.

Sections IV and V below describe the analysis for each nucleon decay mode that we studied. In each case, the particular characteristics of the decay are reviewed and the kinematic cuts designed to eliminate background are presented. The signal and background events which pass the cuts are then tallied. Then, using the mode detection efficiency and detector total exposure, a lifetime limit  $\tau/B$  at 90% confidence level is calculated.

Decay Mode	Hard- ware Trigger	Contain- ment Filter	Event Quality	Topology Selection Scans	Kinem. Cuts	BR	$\epsilon \times \text{BR}$ with INR	$\epsilon \times \text{BR}$ without INR
$p \rightarrow \mu^+ \eta, \eta \rightarrow \gamma\gamma$	0.56	0.56	0.79	0.75	0.94	0.39	$0.07 \pm 0.01$	0.12
$p \rightarrow \mu^+ \eta, \eta \rightarrow \pi^0 \pi^0 \pi^0$	0.57	0.60	0.71	0.81	0.94	0.32	$0.06 \pm 0.01$	0.11
$p \rightarrow e^+ \eta, \eta \rightarrow \gamma\gamma$	0.56	0.62	0.72	0.87	0.94	0.39	$0.08 \pm 0.01$	0.14
$p \rightarrow e^+ \eta, \eta \rightarrow \pi^0 \pi^0 \pi^0$	0.56	0.62	0.71	0.88	0.93	0.32	$0.07 \pm 0.01$	0.12
$n \rightarrow \bar{\nu} \eta, \eta \rightarrow \gamma\gamma$	0.54	0.69	0.70	0.73	0.89	0.39	$0.07 \pm 0.01$	0.12
$n \rightarrow \bar{\nu} \eta, \eta \rightarrow \pi^0 \pi^0 \pi^0$	0.54	0.67	0.63	0.80	0.93	0.32	$0.05 \pm 0.01$	0.09
$n \rightarrow \bar{\nu} \pi^0, \pi^0 \rightarrow \gamma\gamma$	0.45	0.73	0.77	0.57	0.71	1.0	$0.11 \pm 0.01$	0.21
$p \rightarrow \bar{\nu} \pi^+, \pi \rightarrow \mu \rightarrow e$	0.37	0.67	0.88	0.25	0.85	1.0	$0.05 \pm 0.01$	0.10

TABLE I. Survival fractions through event selections applied in succession, for the MC generated nucleon decay final states of this study. The column labeled BR refers to the  $\eta$  or  $\pi$  decay. The effect of intranuclear rescattering (INR) can be seen by comparing the two rightmost columns.

#### IV. SEARCH FOR NUCLEON DECAY INTO $\ell\eta$ AND $\bar{\nu}\eta$

### A. Search for $p \rightarrow \ell^+ \eta$

We have searched for proton decay into  $\mu^+ \eta$  and  $e^+ \eta$  and for neutron decay into  $\bar{\nu} \eta$ . The decay sequences involving the two largest branching modes of the  $\eta$ , namely  $\eta \rightarrow \gamma \gamma$  and  $\eta \rightarrow \pi^0 \pi^0 \pi^0$ , have been investigated. The results from both of these  $\eta$  decay modes are included in the calculation of the limits for all three nucleon decay modes. We also explored the possibility of inclusion of  $\eta \rightarrow \pi^+ \pi^- \pi^0$  and  $\eta \rightarrow \pi^+ \pi^- \gamma$  into our search, but we found the resulting events to be difficult to identify with topology criteria. Since the potential gain is modest, we have not included these processes.

To calculate partial lifetime lower limits,  $\tau/B$ , we use a formalism common to previous analyses by us [8,9] and by the Fréjus tracking calorimeter experiment [14]. The mode  $p \rightarrow \mu^+ \eta$ , the first to be discussed below and which involves two daughter processes for the  $\eta$ , provides an example whose generalization is straightforward:

$$(\tau/B)_{p \rightarrow \mu^+ \eta^0} > N_p \times T_f \times \frac{[\epsilon_1 \times B_1(\eta) + \epsilon_2 \times B_2(\eta)]}{\mu_1 + \mu_2}. \quad (4.1)$$

Here  $N_{p(n)} = 2.87(3.15) \times 10^{32}$  protons (neutrons) in a kiloton of the Soudan 2 detector,  $T_f = 5.52$  kiloton years is the full detector exposure, and  $\epsilon_i \times B_i(\eta)$  are the selection efficiencies given in Table I. The  $\mu_i$  are the constrained 90% CL upper limits on the numbers of observed events, and are found by solving the equation

$$0.10 = \frac{\sum_{n_1=0}^{n_{ev;1}} \sum_{n_2=0}^{n_{ev;2}} P(n_1, b_1 + \mu_1) P(n_2, b_2 + \mu_2)}{\sum_{n_1=0}^{n_{ev;1}} \sum_{n_2=0}^{n_{ev;2}} P(n_1, b_1) P(n_2, b_2)} \quad (4.2)$$

subject to the constraint

$$\frac{\epsilon_1 \times B_1(\eta)}{\mu_1} = \frac{\epsilon_2 \times B_2(\eta)}{\mu_2} = \frac{\sum_{i=1}^2 \epsilon_i \times B_i(\eta)}{\sum_{i=1}^2 \mu_i}. \quad (4.3)$$

In Eq. (4.2),  $P(n, \mu)$  is the Poisson function,  $e^{-\mu} \mu^n / n!$ , and the  $b_i$  are the estimated backgrounds.

### $p \rightarrow \mu^+ \eta$

We have searched for proton decay into  $\mu^+ \eta$ , where the  $\eta$  decays into two photons or into three  $\pi^0$  mesons. With final states involving either of these  $\eta$  decays, the  $\mu^+$  is easily distinguished from the  $\eta$  decay products in the Soudan 2 tracking calorimeter (see Fig. 1). For the  $p \rightarrow \mu^+ \eta$  mode, the  $\mu^+$  momentum is 296 MeV/c in the proton rest frame. In the laboratory frame,  $\mu^+$  momenta are smeared about the two-body nominal value as a result of the Fermi motion of bound protons.

For  $p \rightarrow \mu^+ \eta$ ,  $\eta \rightarrow \gamma \gamma$ , the kinematic region in the invariant mass versus net momentum plane which contains 90% of the reconstructed MC proton decay events, is delineated by the outer contour displayed in Fig. 2. Since the entire final state is visible, the invariant mass will approximate the nucleon mass and the net event momentum will be distributed in accordance with the convolution of Fermi motion with detector resolution. Fig. 2 shows



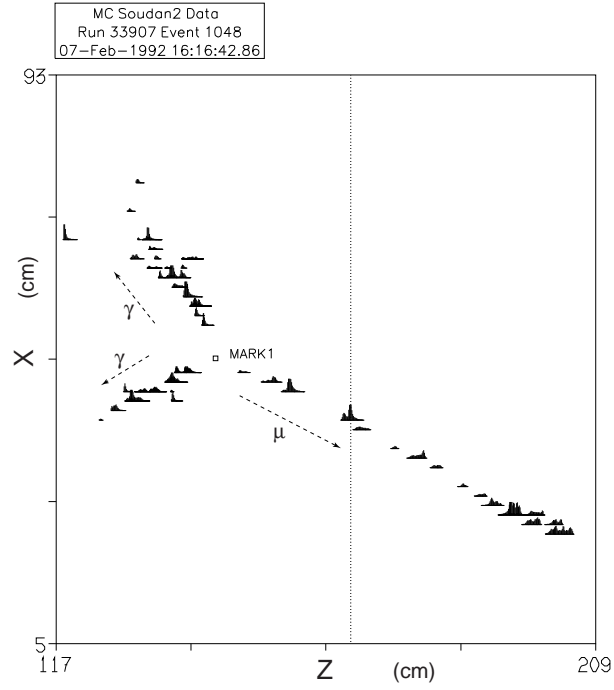


FIG. 1. Monte Carlo event with full detector response for proton decay  $p \rightarrow \mu^+ \eta^0, \eta^0 \rightarrow \gamma\gamma$ . Here, the anode ( $X$ ) versus drift time ( $Z$ ) projection has been selected from the three scanning views with anode-time, cathode-time, and anode-cathode projections. The open square denoted “MARK 1” indicates the reconstructed primary vertex.

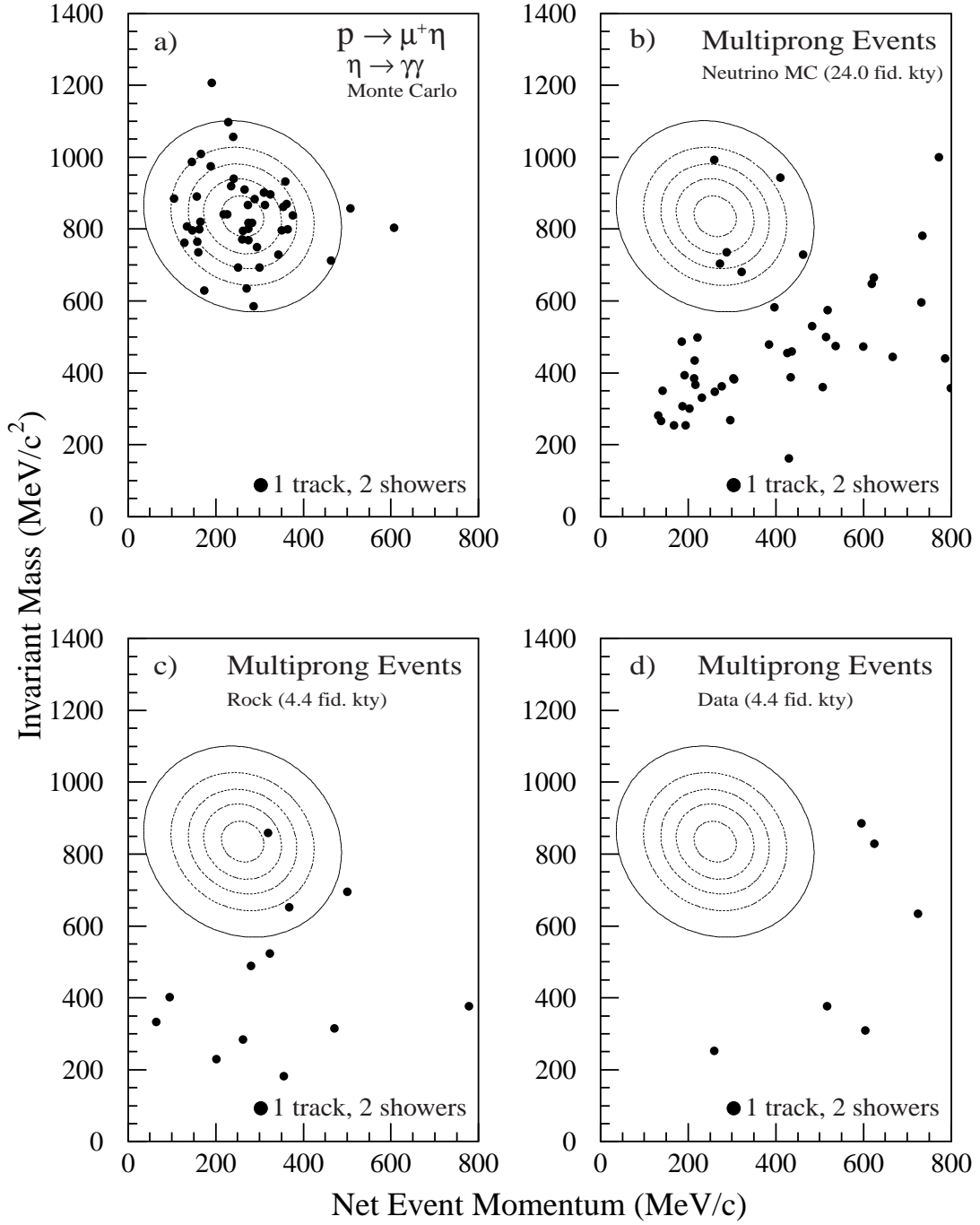


FIG. 2. For  $p \rightarrow \mu^+ \eta$ ,  $\eta \rightarrow \gamma\gamma$ , event samples and the kinematic selection contour in the  $M_{inv}$  versus  $|\vec{p}_{net}|$  plane. The distributions show single track plus two shower events (solid circles) for a) the proton decay simulation, b) the atmospheric neutrino Monte Carlo, c) the rock events, and d) the gold data.

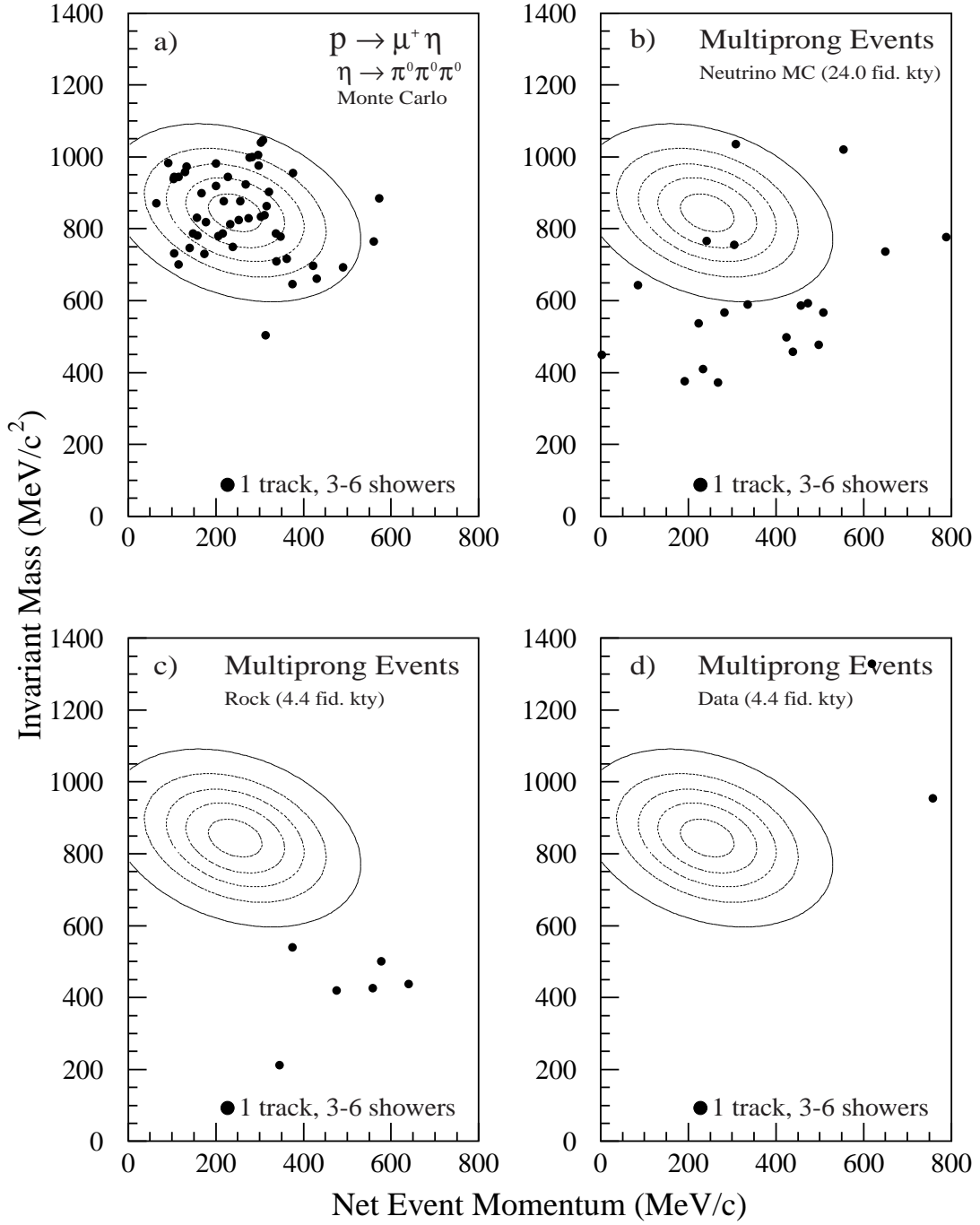


FIG. 3. For  $p \rightarrow \mu^+ \eta$ ,  $\eta \rightarrow \pi^0 \pi^0 \pi^0$ , event samples and kinematic selection contour in the  $M_{inv}$  versus  $|\vec{p}_{net}|$  plane. The distributions show one track plus 3–6 shower events (solid circles) for a) the proton decay simulation, b) the atmospheric neutrino MC, c) the rock events, and d) the gold data events.

the distribution of events within this plane, for the proton decay simulation sample, for the atmospheric neutrino MC sample, and for the rock and gold data samples. The total background which arises from neutrino interactions and from the cosmic ray induced rock events is  $0.9 + 0.1 = 1.0$  events. The neutrino background originates from assorted multiple pion production channels which, after correction for  $\nu_\mu$  oscillations, is comprised of equal portions of  $\nu_\mu$  and  $\nu_e$  inelastic charged-current events.

No events are observed to pass the primary kinematic contour. Due to the small background expectation, no additional kinematic constraints (e.g. on the momentum of the  $\eta$  or the  $\mu^+$ ) were applied. With an overall detection efficiency of 6.9% we establish a limit of  $\tau/B > 48 \times 10^{30}$  years at 90% CL for this decay sequence.

In the other decay sequence of  $p \rightarrow \mu^+\eta$ , namely  $\eta \rightarrow \pi^0\pi^0\pi^0$ , we search for a decay signature of one track and three to six decay showers from the three  $\pi^0$ s. The vertex is defined as the end of the track from which the showers emerge. In this case, the rate of the rock background is small and the background expectation of 0.5 events arises almost entirely from atmospheric neutrino interactions. Fig. 3 shows the kinematic search regions in the  $M_{inv}$  versus  $|\vec{p}_{net}|$  plane, together with the event distributions from the four samples. The detection efficiency for this decay sequence is 5.9%. No data events are observed to pass the kinematic cuts. The limit for this decay sequence is calculated to be  $\tau/B > 41 \times 10^{30}$  years at 90% CL. Combining the two daughter processes we obtain an overall limit of  $\tau/B > 89 \times 10^{30}$  years at 90% CL.

$$p \rightarrow e^+\eta$$

For proton decay into  $e^+\eta$  with  $\eta \rightarrow \gamma\gamma$ , we searched for an event topology of three distinct showers emanating from a common vertex. We found it was not advantageous to distinguish the primary positron shower from the decay photons of the  $\eta$ ; rather, an overall search in the  $M_{inv}$  versus  $|\vec{p}_{net}|$  plane was conducted. Fig. 4 shows all three-shower events and their relation to the kinematic cut region for the proton decay MC, atmospheric neutrino Monte Carlo, rock, and gold data samples. The total background estimate is 0.9 events, of which 0.7 events are calculated to be initiated by atmospheric neutrinos. The background events are mostly due to  $\nu_e$  and  $\bar{\nu}_e$  inelastic charged current interactions. The number of nucleon decay candidates observed is one event. From this we deduce a partial lifetime limit of  $\tau/B > 38 \times 10^{30}$  years at 90% CL.

For the  $\eta \rightarrow \pi^0\pi^0\pi^0$  mode, the signal topology is taken to be four to seven showers, all emerging from a common vertex. The detection efficiency is calculated to be 6.5%. As with  $\eta \rightarrow \gamma\gamma$ , no attempt is made to identify which of the several showers in the event was from the prompt positron. Distributions for this mode are depicted in Fig. 5. Most of the background expectation of 0.6 events can be attributed to  $\nu_e$  charged current multiple  $\pi^0$  production. No data events were observed to pass the kinematic cuts for this mode, and we obtain a limit of  $\tau/B > 48 \times 10^{30}$  years at 90% CL. Combining the two  $\eta$  decay modes gives an overall limit for  $p \rightarrow e^+\eta$  of  $\tau/B > 81 \times 10^{30}$  years at 90% CL.

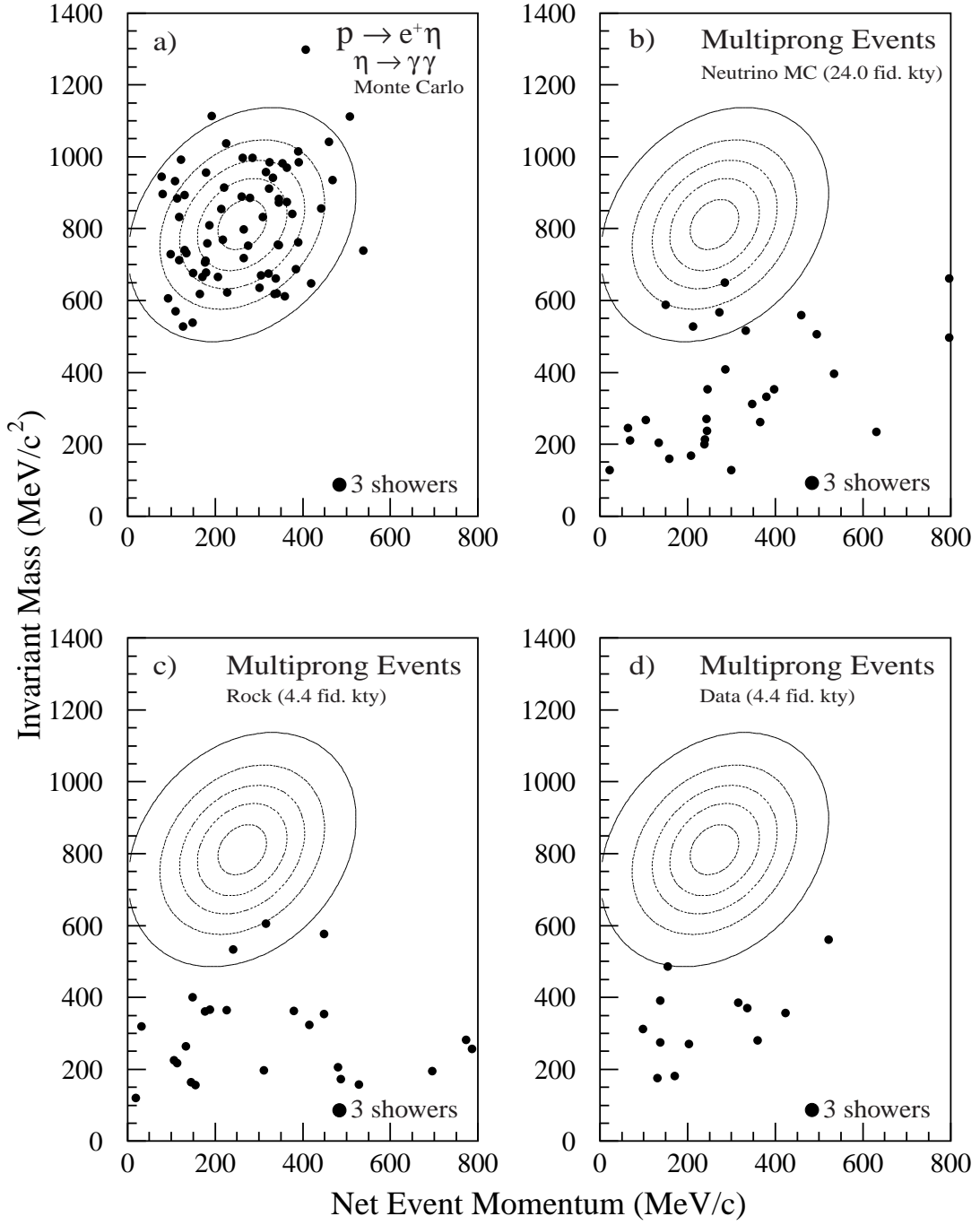


FIG. 4. For  $p \rightarrow e^+\eta$ ,  $\eta \rightarrow \gamma\gamma$ , event samples and kinematic selection contour in the  $M_{inv}$  versus  $|\vec{p}_{net}|$  plane. Distributions show a) the proton decay simulation, b) three-shower events of the atmospheric neutrino MC, c) three-shower rock events, and d) three-shower events of gold data.

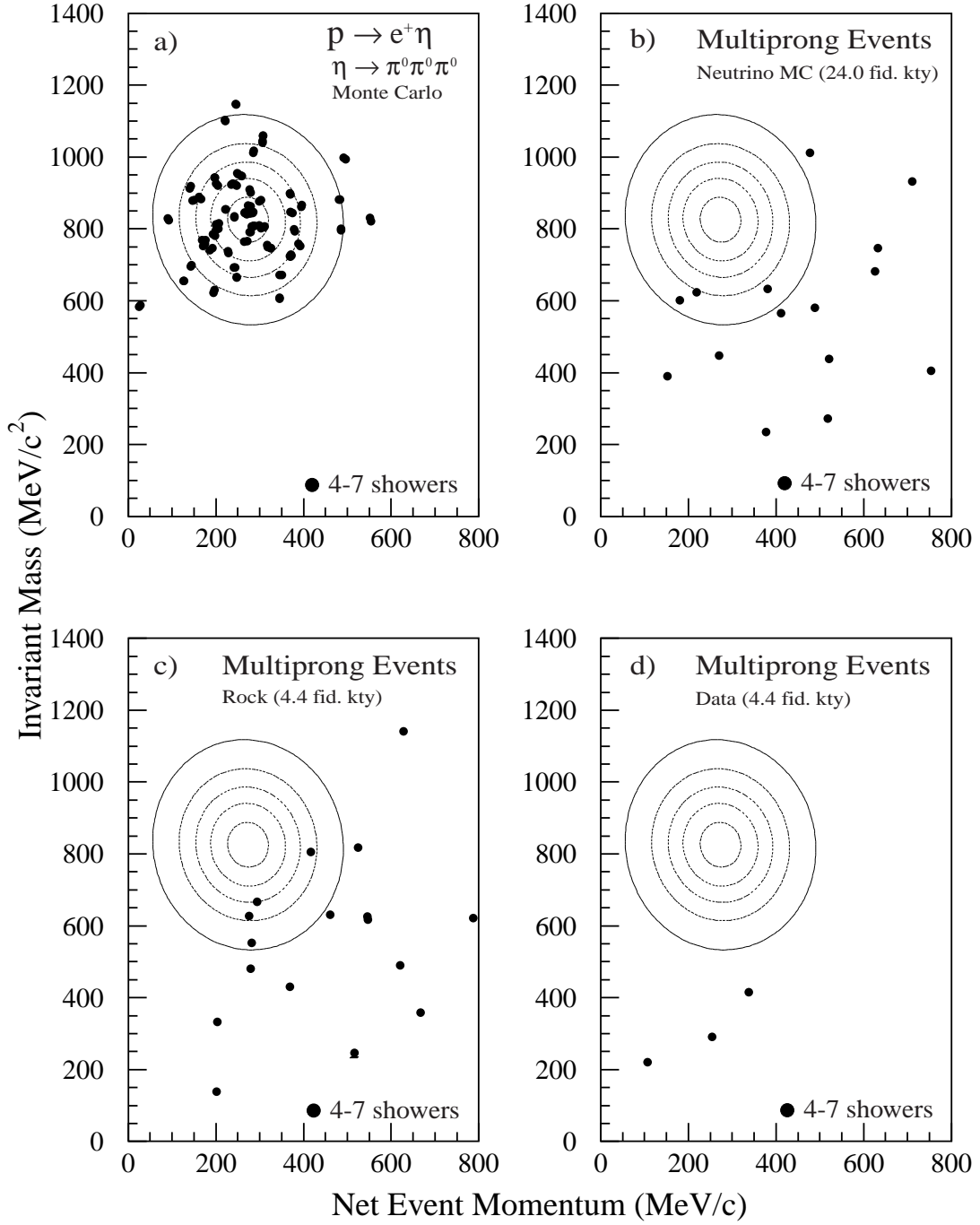


FIG. 5. For  $p \rightarrow e^+\eta$ ,  $\eta \rightarrow \pi^0\pi^0\pi^0$ , event samples and kinematic selection contour in the  $M_{inv}$  versus  $|\vec{p}_{net}|$  plane. Distributions show a) the proton decay simulation, b) 4–7 shower events of the atmospheric neutrino MC, c) 4–7 shower rock events, and d) 4–7 shower events of gold data.

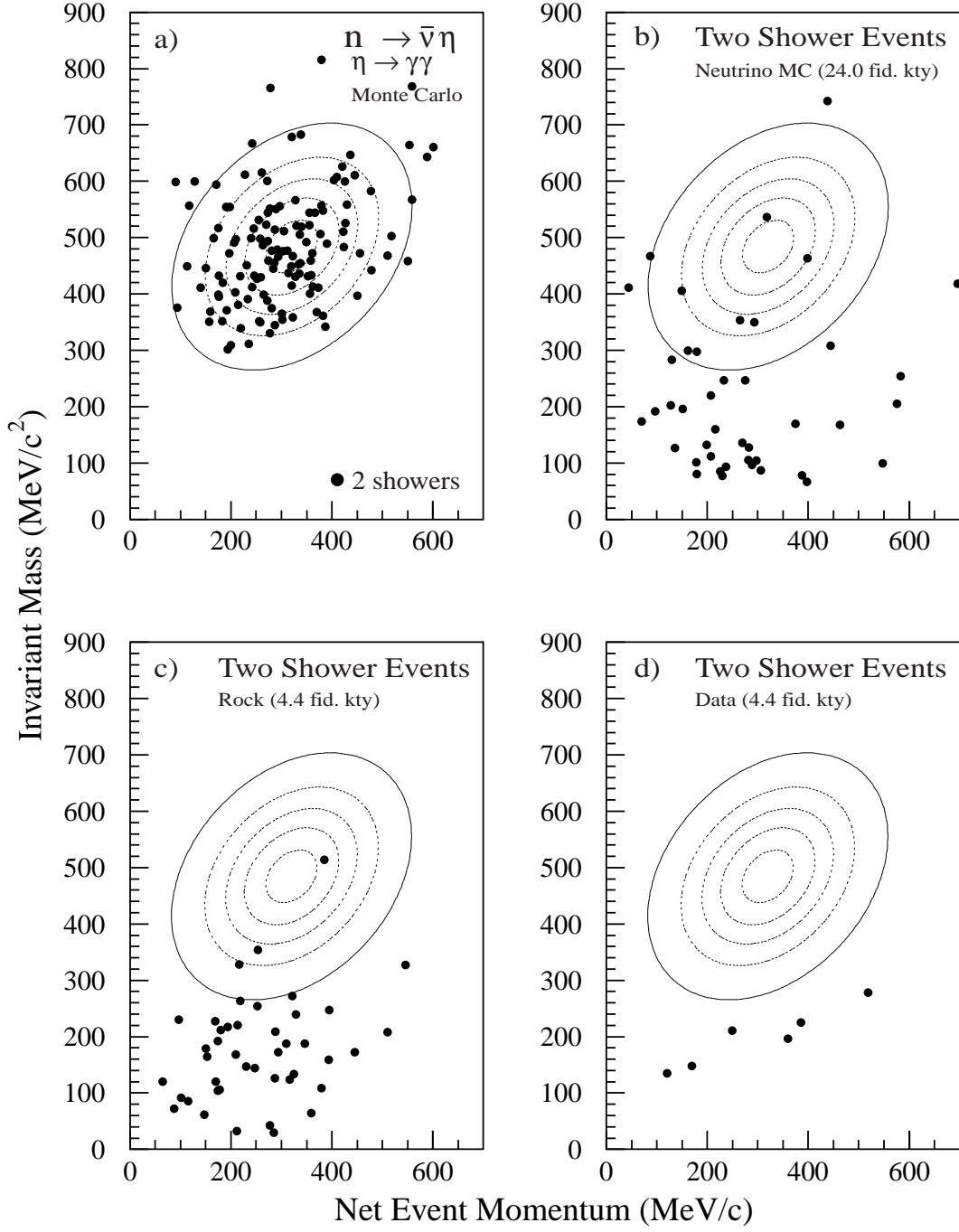


FIG. 6. For  $n \rightarrow \bar{\nu}\eta$ ,  $\eta \rightarrow \gamma\gamma$ , event samples and kinematic selection contour in the  $\gamma\gamma$   $M_{inv}$  versus  $|\vec{p}_{net}|$  plane. Distributions show a) the neutron decay simulation, b) two-shower events of the atmospheric neutrino MC, c) two-shower events of the shield-tagged “rock” sample, and d) two-shower events of gold data.

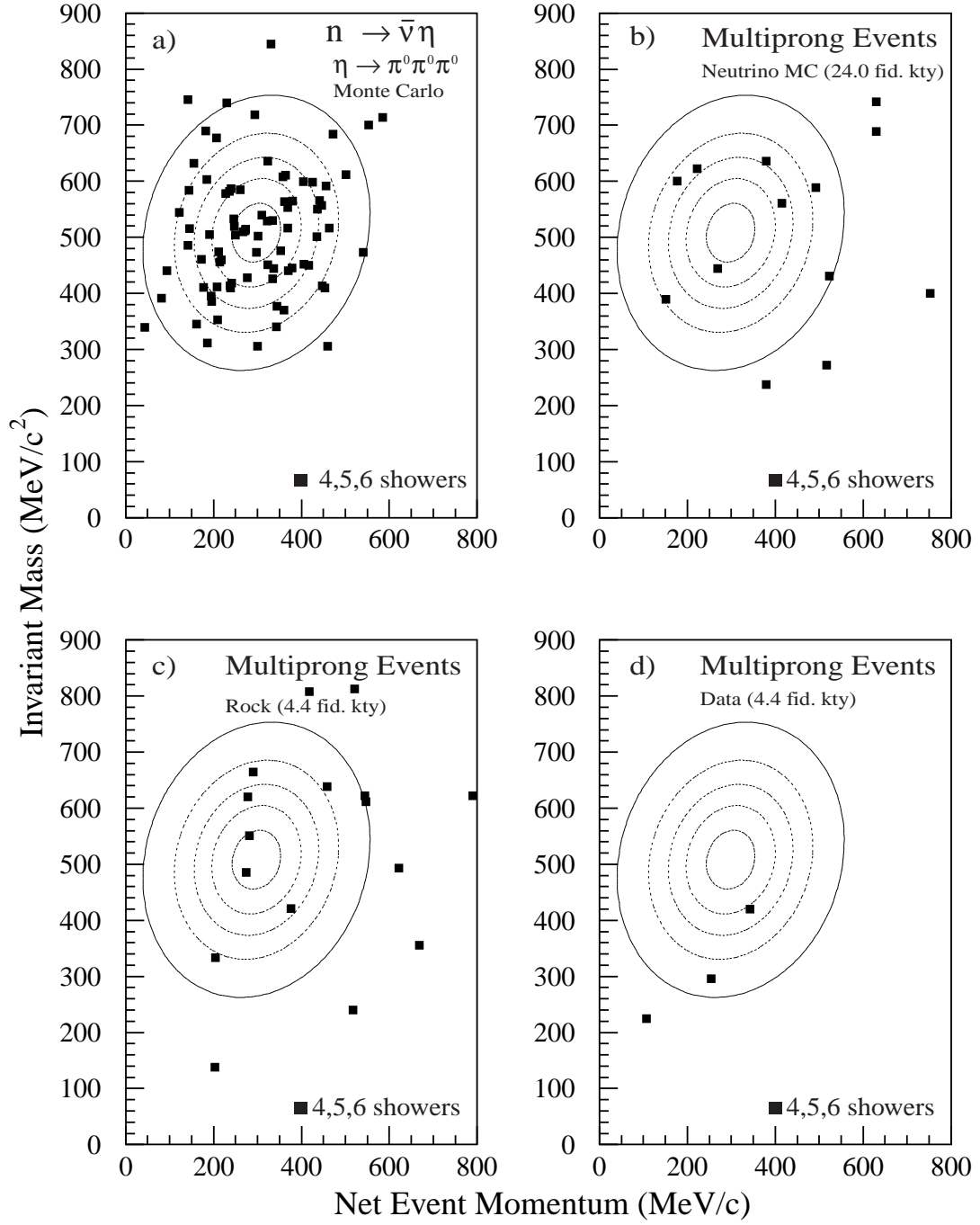


FIG. 7. For  $n \rightarrow \bar{\nu}\eta$ ,  $\eta \rightarrow \pi^0\pi^0\pi^0$ , event samples and kinematic selection contour in the  $M_{inv}$  versus  $|\vec{p}_{net}|$  plane. Distributions show a) the nucleon decay simulation, b) 4-6 shower events of the atmospheric neutrino MC, c) 4-6 shower rock events, and d) 4-6 shower events of gold data.



## $n \rightarrow \bar{\nu}\eta$

Neutron decay  $n \rightarrow \bar{\nu}\eta$  with  $\eta \rightarrow \gamma\gamma$  involves a two-shower final state originating from a “sharp” invariant mass of  $547 \text{ MeV}/c^2$ . We define for  $n \rightarrow \bar{\nu}\eta$ ,  $\eta \rightarrow \gamma\gamma$ , a kinematically-allowed elliptical region in the  $m_{\gamma\gamma}$  versus  $|\vec{p}_{net}|$  plane, as shown in Fig. 6. The four diplots of Fig. 6 show the effect of the kinematic contour selection on the neutron decay simulation (Fig. 6a) and on the two-shower events from the atmospheric neutrino MC, from the rock event sample, and from the gold data. The kinematic contour selection is satisfied by 90% of the MC  $\bar{\nu}\eta$  events, whereas the neutrino and rock backgrounds are almost entirely eliminated. With the loss due to intranuclear rescattering, our detection efficiency for  $n \rightarrow \bar{\nu}\eta$ ,  $\eta \rightarrow \gamma\gamma$  becomes 7%. For this mode, there are no candidate events. The background from neutrino and from rock events is estimated to be 1.7 events. Nearly half of the neutrino-induced background arises from neutral-current production of  $\eta$  and  $\pi^0$ 's. A significant contribution also arises from  $\nu_e$  charged current single  $\pi^0$  production events in which one of the showers is not discernible in scanning. For  $n \rightarrow \bar{\nu}\eta_{\gamma\gamma}$  we obtain a partial lifetime lower limit of  $\tau/B > 53 \times 10^{30}$  years at 90% CL.

For the other  $\eta$  decay mode considered,  $\eta \rightarrow \pi^0\pi^0\pi^0$ , the signal topology is four to six showers emerging from a common vertex. The detection efficiency for  $n \rightarrow \bar{\nu}\eta_{\pi^0\pi^0\pi^0}$  is 5.4% including the intranuclear correction. The distributions in the plane of  $M_{inv}$  versus  $|\vec{p}_{net}|$  are depicted in Fig. 7. From Fig. 7b, the total neutrino background is estimated to be 1.5 events, of which nearly half is  $\nu_e$  charged current interactions with multiple pion production. The remaining background is due to inelastic neutral current interactions. Another 0.6 events are expected from rock events, bringing the total background expectation to 2.0 events. We observe two data events and this gives a partial lifetime limit of  $\tau/B > 22 \times 10^{30}$  years at 90% CL. Combining the two submodes together yields a limit for  $n \rightarrow \bar{\nu}\eta$  of  $\tau/B > 71 \times 10^{30}$  years at 90% CL.

## V. SEARCH FOR $N \rightarrow \bar{\nu}\pi^0$ AND $P \rightarrow \bar{\nu}\pi^+$

We have searched for the two-body nucleon decay modes which yield a final-state (anti-)neutrino together with a  $\pi$ -meson. For the neutron decay into  $\bar{\nu}\pi^0$ , the observable final state consists of two photon showers having a restricted invariant mass, and discrimination from background can be carried out similarly to  $n \rightarrow \bar{\nu}\eta$ ,  $\eta \rightarrow \gamma\gamma$ .

For proton decay into  $\bar{\nu}\pi^+$ , the observable final state is simply a single charged track which can scatter and/or range to stopping with an endpoint decay ( $\pi^+ \rightarrow \mu^+ \rightarrow e^+$ ). A restricted allowed range of pion momentum is implied by the two-body nature of this proton decay. However, the background from quasi-elastic  $\nu_\mu$  and  $\bar{\nu}_\mu$  neutrinos with unobserved proton and neutron recoils is substantial, since muon tracks are indistinguishable from  $\pi^+$  tracks in the Soudan calorimeter, unless of course a distinct scatter is present. Consequently, for the  $p \rightarrow \bar{\nu}\pi^+$  search reported below, we require that an endpoint decay be present on candidate single track events. This requirement discriminates against the background from quasi-elastic  $\nu_\mu n \rightarrow \mu^- p$  reactions (though  $\bar{\nu}_\mu p \rightarrow \mu^+ n$  background still remains).

$$\mathbf{n} \rightarrow \bar{\nu}\pi^0$$

Neutron decay into  $\bar{\nu}\pi^0$  yields a two-shower final state. The invariant mass values obtained by reconstructing event shower pairs from the nucleon decay MC simulation comprise the  $y$ -coordinates of the events shown in Fig. 8a. The  $\gamma\gamma$  mass distribution peaks close to the  $\pi^0$  mass, however it is rather broad (a mean of  $142 \text{ MeV}/c^2$  with a sigma of  $45 \text{ MeV}/c^2$  from a Gaussian fit). For  $\bar{\nu}\pi^0$ , a bi-variate Gaussian does not provide a good characterization of the event distribution in the  $M_{inv}$  versus  $|\vec{p}_{net}|$  plane. For the purpose of accommodating the data, a two-dimensional Gaussian was multiplied by a sigmoid function (a smoothed step function). In fitting the data, parameters governing the orientation of the sigmoid and the slope of its step were allowed to vary, in addition to the parameters of the Gaussian. The result of this fit is the set of contours shown in Fig. 8. As an additional constraint, we require that the two showers have an opening angle less than  $90^\circ$ . Events which are thereby eliminated are shown as open circles in Fig. 8.

In our  $\mathbf{n} \rightarrow \bar{\nu}\pi^0$  simulation, 86% of events lie within the outer contour of Fig. 8a and also satisfy the  $\gamma\gamma$  opening angle requirement. The overall detection efficiency for this mode is 11%. For a simulation in which the intranuclear effects are not included we find a detection efficiency of 21%. The bulk of the INR losses can be attributed to intranuclear absorption and inelastic scattering processes which lower the trigger rate for the simulation from 87% to 45%. A similar INR effect is observed for  $\mathbf{p} \rightarrow \bar{\nu}\pi^+$ .

For  $\mathbf{n} \rightarrow \bar{\nu}\pi^0$  we calculate that 3.8 background events are expected, with 0.9 events from rock processes and 2.9 events from neutrino background. Inspection of the neutrino background reveals that 75% of the events are neutral-current inelastic single  $\pi^0$  production events in which the recoil baryon is either a neutron that escapes detection or a proton that is produced below threshold. The remaining 25% of the background is due to  $\nu_e$  charged-current single charged pion production events in which the pion is misidentified as a shower and recoil baryons are undetected. In the gold data we observe 4 candidate events. The background-subtracted lifetime lower limit at 90% CL is then  $\tau/B > 39 \times 10^{30}$  years.

$$\mathbf{p} \rightarrow \bar{\nu}\pi^+$$

The two-body decay  $\mathbf{p} \rightarrow \bar{\nu}\pi^+$ , of an unbound stationary proton would produce a  $\pi^+$  with a momentum of  $459 \text{ MeV}/c$ . In the Soudan 2 calorimeter, however, protons are mostly to be found within iron nuclei. Pions which are created inside such a nucleus can undergo intranuclear rescattering before they emerge; and, even if they emerge with their identity intact, the  $\pi^+$  mesons traverse a dense medium where they can undergo (further) large energy degradation due to scattering processes. The net result is that  $\pi^+$  mesons of this decay mode exhibit only half of their initial momentum on average, as can be seen from the result of our full simulation shown in Fig. 9a. For our search we require candidate events to have one and only one track (no recoil proton or neutron) with ionization compatible with a pion or muon mass assignment. The pion momentum as reconstructed from range is required to fall within  $140$  to  $420 \text{ MeV}/c$ . Additionally, the track is required to have a visible endpoint decay consisting of two or more decay shower hits. These cuts reduce the final-state

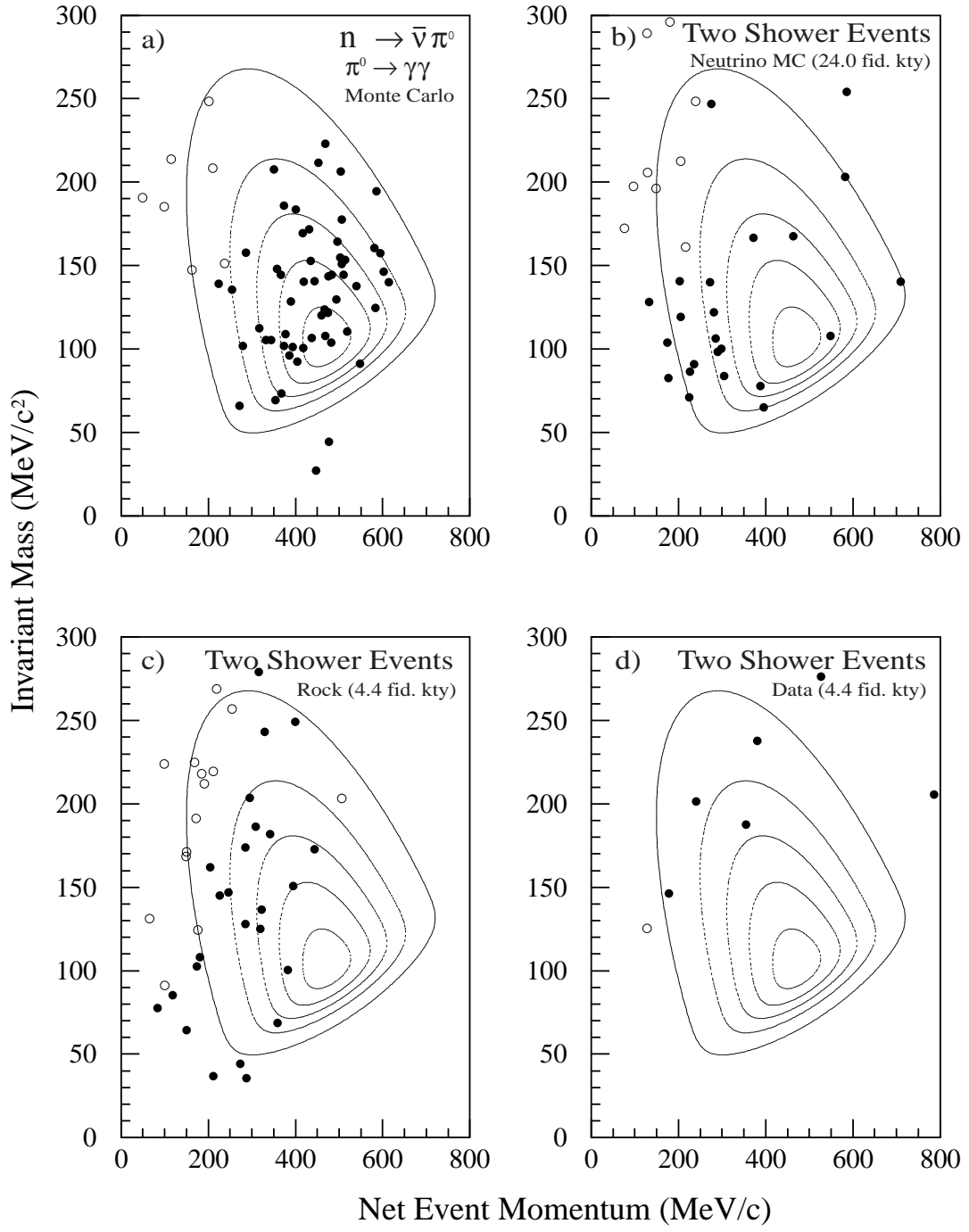


FIG. 8. For  $n \rightarrow \bar{\nu} \pi^0$ , event samples and kinematic selection contour in the  $M_{inv}$  versus  $|\vec{p}_{net}|$  plane. Distributions show two shower events (a) of the nucleon decay simulation, (b) of the atmospheric neutrino MC, (c) of the shield-tagged rock events, and (d) of gold data. Events depicted with solid circles satisfy an angular separation requirement on the gamma showers.

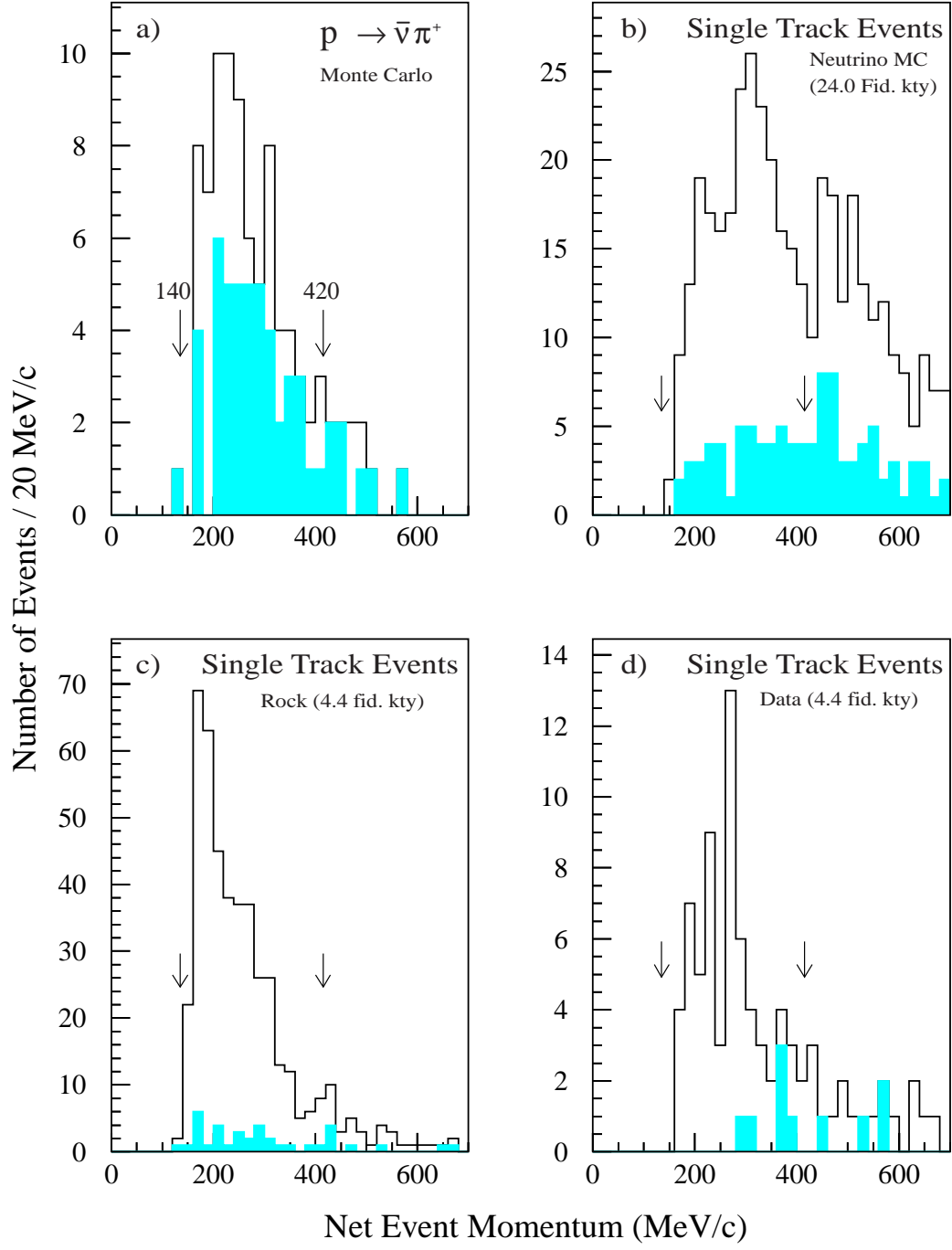


FIG. 9. For  $p \rightarrow \bar{\nu}\pi^+$ , the track momentum distribution from a) the proton decay simulation, b) single track events of the atmospheric neutrino MC, c) single track rock events, and d) single track events of gold data. Events having visible endpoint decays on candidate tracks are shown with shaded histogramming.

detection efficiency by roughly 50% but remove enough of the neutrino background rate to make a search feasible. The total detection efficiency for this mode is 4.6%.

To gauge the effects on efficiency of intranuclear rescattering within the parent nuclei of the calorimeter medium, a proton decay simulation that does not include intranuclear effects has been compared with the full simulation. We observe that the trigger efficiency increases from 47% to 72% in the absence of intranuclear effects. Additionally, the average momentum of the reconstructed pions of the simulation increases from 284 MeV/ $c$  to 356 MeV/ $c$ . Evidently, part of the discrepancy between the predicted two body decay momentum of 459 MeV/ $c$  and the average momentum of the reconstructed pion tracks of the simulation can be attributed to intranuclear scattering. Hadronic scattering processes in the detector medium account for the remaining difference. Finally, in the absence of intranuclear effects, the overall efficiency for  $p \rightarrow \bar{\nu}\pi^+$  would be increased from 4.6% to 8.8%.

With the cuts optimized as described above, we observe 6 candidate events and we estimate the background to be 10.5 events in the absence of oscillations by atmospheric neutrinos. However, in the presence of atmospheric  $\nu_\mu \rightarrow \nu_\tau$  oscillations, our background estimate must be scaled by the Soudan-2 flavor ratio (see Section IIC) and is thereby reduced to 7.7 events. The lifetime lower limit at 90% CL is then  $\tau/B > 16 \times 10^{30}$  years.

## VI. UNCERTAINTIES AND LIFETIME LIMITS

The lifetime lower limits reported here are affected by statistical and systematic uncertainties which arise with detection of each nucleon decay final state and with background estimation. The various error sources, and the corresponding fractional variation  $\Delta\tau_N/\tau_N$  thereby introduced, are similar to those detailed for our lepton +  $K^0$  modes search in Soudan 2 (see Ref. [9], Sect. V). The one exception lies with treatment of intranuclear rescattering losses within parent nuclei for the  $\eta$  and  $\pi$  modes studied here. In contrast to produced  $K^0$ s (strangeness = +1), eta mesons and pions may have sizeable rescattering probability for which there is also significant uncertainty. Based upon uncertainties which arise in our phenomenological cascade model [26], with extrapolation to heavier nuclei of pion production observed in  $\nu_\mu$  deuteron ( $A = 2$ ) and  $\nu_\mu$  neon ( $A = 20$ ) reactions [27], we estimate an uncertainty of 30% for our rescattering treatment. This error is to be added in quadrature to the errors (see below) listed for individual channel detection efficiencies,  $\epsilon \times BR$ , in Table I. As can be seen from equation (4.1), the INR uncertainty enters directly into  $\Delta\tau_N/\tau_N$  via the detection efficiencies  $\epsilon_i$ .

For each channel there is accumulated error on the survival efficiency through selections imposed by triggering, software filtering, scanning, and kinematic cuts; this can be as large as 18%, as indicated by the next-to-rightmost column in Table I. For the  $\bar{\nu}\pi$  modes, and also for  $\bar{\nu}\eta$ , errors enter the lifetime limit through the estimates of background from atmospheric neutrino events and from cosmic ray induced rock events. Propagation of background errors through relations (4.1), (4.2), and (4.3) for individual channels gives  $\Delta\tau_N/\tau_N \leq 20\%$ . We conclude that the uncertainty  $\Delta\tau_N/\tau_N$  on the lifetime lower limits reported in this work may be as large as 40%. Of course, comparable uncertainties also apply to other published limits on the nucleon lifetime.

## VII. SUMMARY AND CONCLUSIONS

A search for five distinct lepton +  $\eta(\pi)$  nucleon decay channels has been carried out using a fiducial exposure of 4.4 kiloton-years recorded by the Soudan 2 fine-grained iron tracking calorimeter. The modes considered are among those proposed in supersymmetric grand unified models. For each mode, cuts have been designed which minimize cosmic-ray neutrino-, photon- and hadron-induced background while maintaining sufficient detection efficiency to allow a sensitive search. From among all of the lepton + pseudoscalar meson modes investigated, zero or small numbers of candidate events are observed; in every case the occurrence of candidates is compatible with expectations for background. A summary of our partial lifetime lower limits  $\tau/B$  at 90% CL obtained with each channel is given in Table II.

Decay Mode	Final State	$\epsilon \times \text{B.R.}$	Background			Data	$N_{90}$	$\tau/B \times 10^{30}y$
			$\nu$	Rock	Total			
$p \rightarrow \mu^+ \eta$	$\gamma\gamma$	0.07	0.9(1.1)	0.1	1.0	0	2.3	89
$p \rightarrow \mu^+ \eta$	$\pi^0 \pi^0 \pi^0$	0.06	0.5(0.6)	$< 0.06$	0.6	0		
$p \rightarrow e^+ \eta$	$\gamma\gamma$	0.08	0.7	0.1	0.9	1	2.9	81
$p \rightarrow e^+ \eta$	$\pi^0 \pi^0 \pi^0$	0.07	0.6	0.2	0.8	0		
$n \rightarrow \bar{\nu} \eta$	$\gamma\gamma$	0.07	1.5	0.2	1.7	0	2.9	71
$n \rightarrow \bar{\nu} \eta$	$\pi^0 \pi^0 \pi^0$	0.05	1.5	0.6	2.0	2		
$n \rightarrow \bar{\nu} \pi^0$	$\gamma\gamma$	0.11	2.9	0.9	3.8	4	4.8	39
$p \rightarrow \bar{\nu} \pi^+$	$\pi^+$	0.05	5.0(8.8)	1.7	7.7	6	4.0	16

TABLE II. Background-subtracted lifetime lower limits at 90% confidence level from Soudan 2. Atmospheric  $\nu_\mu$  depletion due to neutrino oscillations has discernible effect for neutrino background to  $p \rightarrow \bar{\nu} \pi^+$ , and also to  $p \rightarrow \mu^+ \eta$ ; background rates for null oscillations are shown in parentheses.

A comparison of our current Soudan 2 limits with results published by the Fréjus, Kamiokande, and IMB-3 experiments is presented in Table III. For the two-body lepton-plus-eta decay modes  $p \rightarrow \mu^+ \eta$ ,  $p \rightarrow e^+ \eta$ , and  $n \rightarrow \bar{\nu} \eta$ , we observe zero, one, and two candidates respectively, with comparable expectations for background processes. Our resulting lifetime lower limits are compatible with those listed by the Particle Data Group [30] and are the most stringent limits achieved using iron calorimeters.

Decay Mode	$\tau/B$ ( $10^{30}$ years)			
	Soudan 2	Fréjus [14,15]	Kamiokande [12]	IMB-3 [16]
$p \rightarrow \mu^+ \eta$	89	26	69	126
$p \rightarrow e^+ \eta$	81	44	140	313
$n \rightarrow \bar{\nu} \eta$	71	29	54	158
$n \rightarrow \bar{\nu} \pi^0$	39	13	100	112
$p \rightarrow \bar{\nu} \pi^+$	20	10	25	10

TABLE III. Comparison of 90% confidence level background-subtracted limits in nucleon decay experiments.

### ACKNOWLEDGEMENTS

This work was supported by the U.S. Department of Energy, the U.K. Particle Physics and Astronomy Research Council, and the State and University of Minnesota. We wish to thank the Minnesota Department of Natural Resources for allowing us to use the facilities of the Soudan Underground Mine State Park.

## REFERENCES

- [1] P. Nath, A. H. Chamseddine, and R. Arnowitt, Phys. Rev. **D 32**, 2348 (1985).
- [2] J. Hisano, H. Murayama, and T. Yanagida, Nucl. Phys. **B 402**, 46 (1993).
- [3] P. Nath, R. Arnowitt, “*Grand Unification and B & L Conservation*”, e-print hep-ph/9808465.
- [4] A.L. Macpherson, Nucl. Phys. **B 472**, 79 (1996).
- [5] V. Lucas and S. Raby, Phys. Rev. **D 55**, 6986 (1997).
- [6] K.S. Babu, J.C. Pati, and F. Wilczek, Phys. Lett. **B 423**, 337 (1998).
- [7] J.C. Pati, Int. J. Mod. Phys. **A 14**, 2949 (1999).
- [8] *Soudan 2 Collaboration*, W.W.M. Allison *et al.*, Phys. Lett. **B 427**, 217 (1998).
- [9] *Soudan 2 Collaboration*, D. Wall *et al.*, “Search for nucleon decay into lepton +  $K^0$  final states using Soudan 2”, hep-ex/9910026, accepted for publication in Phys. Rev. D.
- [10] *IMB Collaboration*, H.S. Park *et al.*, Phys. Rev. Lett. **54**, 22 (1985).
- [11] *IMB Collaboration*, S. Seidel *et al.*, Phys. Rev. Lett. **61**, 2522 (1988).
- [12] *Kamiokande Collaboration*, K.S. Hirata *et al.*, Phys. Lett. **B 220**, 308 (1989).
- [13] *HPW Collaboration*, T.J. Phillips *et al.*, Phys. Lett. **B 224**, 348 (1989).
- [14] *Fréjus Collaboration*, Ch. Berger *et al.*, Nucl. Phys. **B 313**, 509 (1989).
- [15] *Fréjus Collaboration*, Ch. Berger *et al.*, Z. Phys. **C 50**, 385 (1991).
- [16] *IMB-3 Collaboration*, C. McGrew *et al.*, Phys. Rev. **D 59**, 052004 (1999).
- [17] *Soudan 2 Collaboration*, W.W.M. Allison *et al.*, Nucl. Instr. Meth. **A 376**, 36 (1996); *Ibid*, **A 381**, 385(1996).
- [18] *Soudan 2 Collaboration*, W.P. Oliver *et al.*, Nucl. Instr. Meth. **A 276**, 371 (1989).
- [19] T.K. Gaisser, T. Stanev, and G. Barr, Phys. Rev. **D 38**, 85 (1988); G. Barr, T.K. Gaisser, T. Stanev, Phys. Rev. **D 39**, 3532 (1989).
- [20] *Soudan 2 Collaboration*, W.W.M. Allison *et al.*, Phys. Lett. **B 391**, 491 (1997).
- [21] W. Leeson *et al.*, Soudan 2 internal note PDK-684, 1997 (unpublished).
- [22] *Super-Kamiokande Collaboration*, Y. Fukuda *et al.*, Phys. Lett. **B 433**, 9 (1998); Phys. Rev. Lett. **81**, 1562 (1998); Phys. Lett. **B 436**, 33 (1998).
- [23] W.A. Mann, plenary talk at the XIXth Int. Symposium on Lepton and Photon Interactions at High Energies, Stanford University, Aug. 1999, hep-ex/9912007 (to be published).
- [24] *Soudan 2 Collaboration*, W.W.M. Allison *et al.*, Phys. Lett. **B 449**, 137 (1999).
- [25] A. Bodek and J.L. Ritchie, Phys. Rev. **D 23**, 1070 (1981).
- [26] W.A. Mann *et al.*, Soudan 2 internal note PDK-377, 1988 (unpublished); W. Leeson *et al.*, Soudan 2 internal note PDK-678, 1997 (unpublished).
- [27] R. Merenyi *et al.*, Phys. Rev. **D 45**, 743 (1992); R. Merenyi, Ph.D. thesis, Tufts University, 1990.
- [28] M. Effenberger and A. Sibirtsev, Nucl. Phys. **A 632**, 99 (1998).
- [29] D. Wall, Ph.D. Thesis, Tufts University, 1998.
- [30] C. Caso *et al.*, “*Review of particle physics*”, Eur. Phys. J. **C 3**, 1 (1998).